

## Data-driven Optimisation of Closure Coefficients of a Turbulence Model

*Andrea Da Ronch*  
*University of Southampton*  
*Lecturer*  
*Southampton, SO17 1BJ, UK*  
[a.da-ronch@soton.ac.uk](mailto:a.da-ronch@soton.ac.uk)

*Marco Panzeri*  
*Noesis Solutions N.V.*  
*Research Engineer*  
*3001 Leuven, Belgium*

*Jernej Droljnik*  
*University of Southampton*  
*Research Associate*  
*Southampton, SO17 1BJ, UK*

*Roberto d'Ippolito*  
*Noesis Solutions N.V.*  
*Research and Innovation Manager*  
*3001 Leuven, Belgium*

### ABSTRACT

The solution of the Reynolds-averaged Navier-Stokes equations employs an appropriate set of equations for the turbulence modelling. The closure coefficients of the turbulence model were calibrated using empiricism and arguments of dimensional analysis. These coefficients are considered universal, but there is no guarantee this property applies to test cases other than those used in the calibration process. This work aims at revisiting the universality of the closure coefficients of the original Spalart-Allmaras turbulence model using machine learning, adaptive design of experiments and accessing a high-performance computing facility. The automated calibration procedure is carried out once for a transonic, wall-bounded flow around the RAE 2822 aerofoil. It was found that: a) an optimal set of closure coefficients exists that minimises numerical deviations from experimental data; b) the improved prediction accuracy of the calibrated turbulence model is consistent across different flow solvers; and c) the calibrated turbulence model outperforms slightly the standard model in analysing complex flow features around the ONERA M6 wing. A by-product of this study is a fully calibrated turbulence model that leverages on current state-of-the-art computational techniques, overcoming inherent limitations of the manual fine-tuning process.

**KEYWORDS:** *machine-learning, closure coefficients, calibration, turbulence model, Sobol indices, design of experiments*

### NOMENCLATURE

Latin	$c_{w3}$ – part of $f_w$ function, speeding up the decay rate of the destruction term in the outer region of the boundary layer
$b$ – wing span	$c_{t3}$ – part of $f_{t2}$ function (in production and destruction terms), helping transition prediction
$c$ – mean aerodynamic chord	$c_{t4}$ – part of $f_{t2}$ function (in production and destruction terms), helping transition prediction
$C_D$ – drag coefficient	$c_{b1}$ – calibrates the growth of $\hat{v}$
$C_m$ – pitch moment coefficient	$c_{b2}$ – empirical constant in the turbulence model
$C_N$ – normal force coefficient	
$C_p$ – pressure coefficient	
$c_{v1}$ – coefficient used in turbulent eddy viscosity calculation and production term	



$c_{w2}$  – part of  $g$  function, controlling the slope of  $f_w$  in destruction; calibrated to match skin friction coefficient of flat plate  
 $d$  – distance to the wall  
 $k$  – Von Karman constant  
 $M$  – Mach number  
 $Re$  – Reynolds number  
Greek

$\alpha$  – angle of attack  
 $\rho$  – flow density  
 $\nu$  – molecular kinematic viscosity  
 $\hat{\nu}$  – kinematic turbulent, or eddy, viscosity  
 $\mu$  – molecular dynamic viscosity  
 $\Omega$  – magnitude of the vorticity  
 $\sigma$  – turbulent Prandtl number

## 1 INTRODUCTION

A deterministic computational fluid dynamics (CFD) simulation gives a single solution for a certain set of input parameters, e.g. geometry, freestream flow conditions, etc. In practice, these parameters may be uncertain and the associated variability may have a significant impact on the final results. For this reason, stochastic CFD simulations are needed to assess the uncertainty in the solution and to achieve a certain level of robustness or reliability in the final aerodynamic design. The point-collocation nonintrusive polynomial chaos technique is the method of choice to propagate the uncertainty in CFD simulations, as exemplified in [1] (and references therein). This technique requires less deterministic CFD simulations than Monte Carlo techniques by assuming a polynomial chaos expansion of low degree for the uncertain output variables.

Today, it is apparent that CFD workflows contain considerable uncertainty, often not quantified [2]. Numerical uncertainties in the results come from: a) physical modelling errors and uncertainties, for example, in accurate predictions of turbulent flows; b) numerical errors arising from mesh and discretisation inadequacies; and c) aleatory uncertainties derived from natural variability and epistemic uncertainties due to the lack of knowledge in the parameters of a specific fluid problem. The work presented in the current paper addresses the last aspect, which calls for turbulence modelling uncertainty quantification and sensitivity analysis.

Uncertainty in the closure coefficients of a turbulence model is the dominant source of error in Reynolds-averaged Navier-Stokes (RANS) simulations, but no reliable estimator for this error component exists. Furthermore, there is no consensus on the best values of these coefficients, as suggested by the wide range of values proposed in the open literature [3]. Current efforts to address these concerns use Bayesian approaches. For example, Ref. [4] described a stochastic error estimate of turbulence models based on variability in the model coefficients. In a sensitivity analysis, it was found that Von Karman constant,  $k$ , has the largest impact on uncertainty in  $u^+$  in the log layer of a flat plate boundary layer. This conclusion was suggested analysing results from several turbulence models, including Spalart-Allmaras (SA) [5] and Wilcox  $k - \omega$  models. In [6], a Bayesian inference framework was used to quantify the uncertainty in the SA model due to the uncertainty in the closure coefficients. For a flat plate and a backward-facing step problem, the coefficients  $k$ ,  $c_{v1}$ , and  $c_{b1}$  were found to contribute most to the uncertainty in the SA model for the chosen output quantities of interest. Reference [7] quantified the uncertainty and sensitivity of three turbulence models (SA, Wilcox  $k - \omega$ , and Menter shear-stress transport models) due to uncertainty in the values of closure coefficients for transonic, wall-bounded flows. The analysis was carried out using point-collocation nonintrusive polynomial chaos technique. The test cases were for the flow around an asymmetric bump at zero degrees angle of attack and for Case 6 of the RAE 2822 aerofoil at a prescribed normal force coefficient [8]. For the aerofoil case, the angle of attack was adjusted for each (baseline) turbulence model to match the target normal force coefficient. The same angle of attack was then used in all subsequent simulations where the closure coefficients were modified for uncertainty quantification. Observe that this approach fails to meet the prescribed normal force coefficient for any variation of the closure coefficients from their baseline values. Furthermore, no indications were given on the best values of the closure coefficients for each turbulence model that improved the agreement with experimental data.

The aim of this study is to revisit the universality of the standard values of the closure coefficients commonly employed in the SA turbulence model. The work is structured around three technical objectives. The first objective is to exploit current state-of-the-art machine-learning techniques to assess the sensitivity of the output quantities of interest on the uncertainty in turbulence model closure coefficients. The second objective is to calibrate the closure coefficients of the SA turbulence model by minimising the deviation of numerical results from available experimental data for transonic flows around an aerofoil (RAE 2822). The third objective evaluates the generality of the calibrated SA



turbulence model on different flow solvers and the expected improvements in prediction accuracy for transonic flows around a three-dimensional wing (ONERA M6).

The need for an automated calibration, which overcomes the limitations imposed by a manual tuning, is not a conjecture, but an intrinsic requirement to deliver a complete and usable turbulence model. As an example, ANSYS Fluent<sup>1</sup> informs the user that: "The  $\gamma$  transition model has only been calibrated for classical boundary layer flows. Application to other types of wall-bounded flows is possible, but might require a modification of the underlying correlations."

Uncertainty quantification and sensitivity analyses, and the calibration of the turbulence model closure coefficients, suffer from the curse of dimensionality [9]. In this respect, the reader is invited to reflect upon the work by Sørensen [10]: "Determining the empirical correlations by numerical optimization, along with debugging the model, demands a very large amount of computations, and it is the hope that other researchers can confirm the present expressions by implementation in other flow solvers.". To overcome the large amount of computations, a strategy based on surrogate models is employed. This requires setting up and running a design of experiments (DOE) plan to acquire the relevant information on the system behaviour. A surrogate model that mimics the dependence between the turbulence model closure coefficients and the output quantities of interest is then built and employed to perform the sensitivity analysis and the model calibration. The key aspect of this strategy is to minimise the number of deterministic CFD simulations while maintaining an accurate representation of the system behaviour. In this study, these aspects are encapsulated in an adaptive DOE (ADOE) algorithm that: a) identifies the regions of the design space that are more difficult to model due to strong non-linearities or scarcity of data, for example; b) distributes iteratively the design points in those areas of the design space; and c) selects automatically the surrogate model that best fits the results obtained from the DOE plan. All these features are supported by the machine-learning framework described in [11], where the robustness, efficiency and accuracy of the proposed ADOE algorithm were found to be superior to traditional DOE techniques.

The paper continues in Section 2 with a description of the flow solver and the machine-learning approach used to calibrate the closure coefficients of the SA turbulence model. Then, Section 3 introduces the aerofoil and wing test cases. A discussion of the results is presented in Section 4. Finally, conclusions and future recommendations are given in Section 5.

## 2 METHODS

The computational framework consists of two software tools. The flow solver in Section 2.1 was used for the flow predictions. The uncertainty quantification and sensitivity analysis, and the optimisation of the closure coefficients, were carried out with the software described in Section 2.2.

### 2.1 Flow Solver

The flow solver employed in this study is DLR-Tau [12], a finite volume based CFD flow solver used by several aerospace industries across Europe. The DLR-Tau solver uses an edge-based vertex-centred scheme, where the convective terms are computed via several first- and second-order schemes, including central and upwind types. The viscous terms are computed with a second-order central scheme. Time integration is performed either with various explicit Runge-Kutta schemes or the Lower-Upper Symmetric Gauss-Seidel (LU-SGS) implicit approximate factorisation scheme. For time accurate computations, the dual time stepping approach of Jameson [13] is employed. Convergence is improved with a multi-grid acceleration technique based on agglomerated coarse grids. Several models for turbulence closure are available.

For the SA model [5], the transport equation is

$$\frac{\partial \hat{v}}{\partial t} + u_j \frac{\partial \hat{v}}{\partial x_j} = c_{b1}(1 - f_{t2})\hat{S}\hat{v} - \left[ c_{w1}f_w - \frac{c_{b1}}{k^2}f_{t2} \right] \left( \frac{\hat{v}}{d} \right)^2 + \frac{1}{\sigma} \left[ \frac{\partial}{\partial x_j} \left( (\nu + \hat{\nu}) \frac{\partial \hat{v}}{\partial x_j} \right) + c_{b2} \frac{\partial \hat{v}}{\partial x_i} \frac{\partial \hat{v}}{\partial x_i} \right] \quad (1)$$

The turbulent eddy viscosity is calculated by

$$\mu_t = \rho \hat{\nu} f_{v1} \quad (2)$$

---

<sup>1</sup> ANSYS Fluent User's Guide:

[https://www.sharcnet.ca/Software/Ansys/17.0/en-us/help/flu\\_th/flu\\_th\\_sec\\_turb\\_intermittency\\_over.html](https://www.sharcnet.ca/Software/Ansys/17.0/en-us/help/flu_th/flu_th_sec_turb_intermittency_over.html)



where

$$f_{v1} = \frac{\chi^3}{\chi^3 + c_{v1}^3}; \quad \chi = \frac{\hat{v}}{v}; \quad v = \mu/\rho \quad (3)$$

Furthermore, one has

$$\hat{S} = \Omega + \frac{\hat{v}}{k^2 d^2} f_{v2}; \quad \Omega = \sqrt{2W_{ij} W_{ij}} \quad (4)$$

$$f_{v2} = 1 - \frac{\chi}{1 + \chi f_{v1}}; \quad f_w = g \left[ \frac{1 + c_{w3}^6}{g^6 + c_{w3}^6} \right]^{\frac{1}{6}}; \quad g = r + c_{w2}(r^6 - r) \quad (5)$$

$$r = \min \left[ \frac{\hat{v}}{S \kappa^2 d^2}, 10 \right]; \quad f_{t2} = c_{t3} \exp(-c_{t4} \chi^2); \quad W_{ij} = \frac{1}{2} \left( \frac{\partial u_i}{\partial x_j} - \frac{\partial u_j}{\partial x_i} \right) \quad (6)$$

and

$$c_{w1} = \frac{c_{b1}}{\kappa^2} + \frac{1 + c_{b2}}{\sigma} \quad (7)$$

In its original formulation [5], the SA model includes 11 closure coefficients. In DLR-Tau, the model implementation neglects the trip terms,  $c_{t1}$  and  $c_{t2}$ , which are also passive for the transonic, wall-bounded flows of this study. Herein, nine closure coefficients (after removing  $c_{t1}$  and  $c_{t2}$ ) were varied for the uncertainty quantification and sensitivity analysis. A summary of the SA closure coefficients to be varied and their associated epistemic intervals are reported in Table 1. The choice of the epistemic intervals, some of which differ slightly from [7], lies on empirical suggestions, physical constraints, and experimental evidence [3, 5, 7].

**Table 1: SA closure coefficients and epistemic intervals.**

Parameter	Standard value	Lower bound	Upper bound
$\sigma$	$6.667 \cdot 10^{-1}$	$6.0000 \cdot 10^{-1}$	$1.400 \cdot 10^0$
$\kappa$	$4.100 \cdot 10^{-1}$	$3.6000 \cdot 10^{-1}$	$4.200 \cdot 10^{-1}$
$c_{v1}$	$7.100 \cdot 10^0$	$6.9000 \cdot 10^0$	$7.500 \cdot 10^0$
$c_{w3}$	$2.000 \cdot 10^0$	$1.5000 \cdot 10^0$	$2.750 \cdot 10^0$
$c_{t3}$	$1.200 \cdot 10^0$	$1.0000 \cdot 10^0$	$2.000 \cdot 10^0$
$c_{t4}$	$5.000 \cdot 10^{-1}$	$3.0000 \cdot 10^{-1}$	$7.000 \cdot 10^{-1}$
$c_{b1}$	$1.355 \cdot 10^{-1}$	$1.2893 \cdot 10^{-1}$	$1.400 \cdot 10^{-1}$
$c_{b2}$	$6.220 \cdot 10^{-1}$	$6.0983 \cdot 10^{-1}$	$7.000 \cdot 10^{-1}$
$c_{w2}$	$3.000 \cdot 10^{-1}$	$5.5000 \cdot 10^{-2}$	$3.525 \cdot 10^{-1}$

The choice for using DLR-Tau was made to demonstrate that uncertainty in closure coefficients has been overlooked in the past, even for an industrial-grade software tool. This situation may have arisen for convenience, by removing additional difficulties from the multifaced complexities of CFD algorithmic implementation, or negligence, by treating CFD as an established technique. The present work carries out an investigation into an intrinsic weakness of turbulence modelling, and creates a preliminary background knowledge for a robust engineering design.

## 2.2 Machine-learning Framework

The machine-learning framework is provided by the software platform Noesis Optimus [14]. The framework consists of an iterative ADOE technique that analyses available data, generally produced by previous iterations or previous DOE runs, to distribute the design points of the next iteration in areas of the parameter space considered of interest. The choice of the location of new sample points is driven by two competing factors. The first factor, denoted space-learning, tends to cover uniformly the design space. No information about the response of the model is therefore needed. The second factor, denoted feature-learning, aims at improving the accuracy of the surrogates by identifying critical areas of the design space, such as non-linearities and discontinuities. The reader is referred to Ref. [11] for more details on our implementation of space-learning and feature-learning factors, the associated algorithms, and the relevant benchmark cases (analytical and industrially-relevant). A key aspect of the machine-learning framework, which represents the backbone of the ADOE algorithm, is the capability to identify automatically the best surrogate models for a given set of design points. In the current implementation,



Kriging interpolating models together with linear, cubic and thin-plate radial basis functions are considered. The advantages of the ADOE algorithm consist therefore on the possibility to perform in a completely unsupervised fashion: a) the iterative selection of the design point locations considered in the DOE campaign; and b) the choice of the response surface model type. These features, embedded in Noesis Optimus, are exploited in the current study to assess the sensitivity of the output quantities of interest (flow solution and aerodynamic coefficients) on the uncertainty in the closure coefficients of the SA turbulence model, and to calibrate automatically the values of these coefficients based on available experimental data.

### 3 TEST CASES

Two test cases are considered. The first test case, RAE 2822 aerofoil, is used for uncertainty quantification and sensitivity analysis as well as for the calibration of the closure coefficients. The second test case, ONERA M6 wing, is used to assess the enhanced prediction capability of the calibrated turbulence model in comparison with the standard SA model.

Data supporting this study (grids, results, figures, etc.) are openly available from the University of Southampton repository at <https://doi.org/10.5258/SOTON/D0263>.

#### 3.1 RAE 2822 Aerofoil

Navier-Stokes (NS) calculations for Case 6 of the RAE 2822 aerofoil [8] were performed with the SA turbulence model. The experimental data for this case are for  $M = 0.729$  and  $Re = 6.5 \cdot 10^6$  at a prescribed normal force coefficient  $C_N = 0.743$ . For all calculations, the angle of attack was adjusted to match this value of  $C_N$ . The computational grid adopted for the flow simulations, shown in Figure 1a, is available from the NPARC Alliance Validation Archive web site [15]. The C-grid, denoted hereafter the coarse grid, consists of a single-block with  $369 \times 65$  points. The far-field boundary is placed at about 20 chords from the aerofoil, and the distance of the first grid points off the aerofoil surface is about  $10^{-5}$  chord.

For all steady calculations, the explicit time stepping and the fourth order Runge-Kutta scheme were used. To accelerate the convergence to a steady state, a local time-stepping, implicit residual smoothing and a full multigrid method were used. The discretisation of the convective and diffusive fluxes of both RANS and SA equations is based on the second order Roe's flux difference splitting scheme. Venkatakrishnan's flux limiter was used for all simulations reported in this paper. A no-slip boundary condition was applied on the aerofoil surface, and far-field boundary conditions were applied to the far-field boundaries. The ratio of eddy viscosity to molecular viscosity 0.5 is prescribed at the far-field boundaries, whereas at smooth walls, zero turbulence condition is enforced. The CFL number was set to 1.2 and the number of multigrid (MG) levels to 3. Simulations were run for 4,000 MG cycles to compute the steady state solution. With this setup, the overall residuals of the NS and SA equations decreased by about five orders of magnitude, and all force and moment components converged within 2,000 MG cycles.

For Case 6 ( $M = 0.729$ ,  $Re = 6.5 \cdot 10^6$ , and prescribed  $C_N = 0.743$ ), the angle of attack with the standard SA model was found to be  $\alpha = 2.51^\circ$ , the drag coefficient  $C_D = 0.0150$ , and the pitch moment coefficient about quarter chord  $C_m = -0.0909$ , compared, respectively, with  $2.92^\circ$ ,  $0.0127$ , and  $-0.095$  in the experiment. The comparison of the pressure coefficient distribution with experimental data is shown in Figure 1b. The overall agreement is good, but differences are visible near the leading edge and at the shock front ( $x/c = 0.15$  and  $0.55$ , respectively).

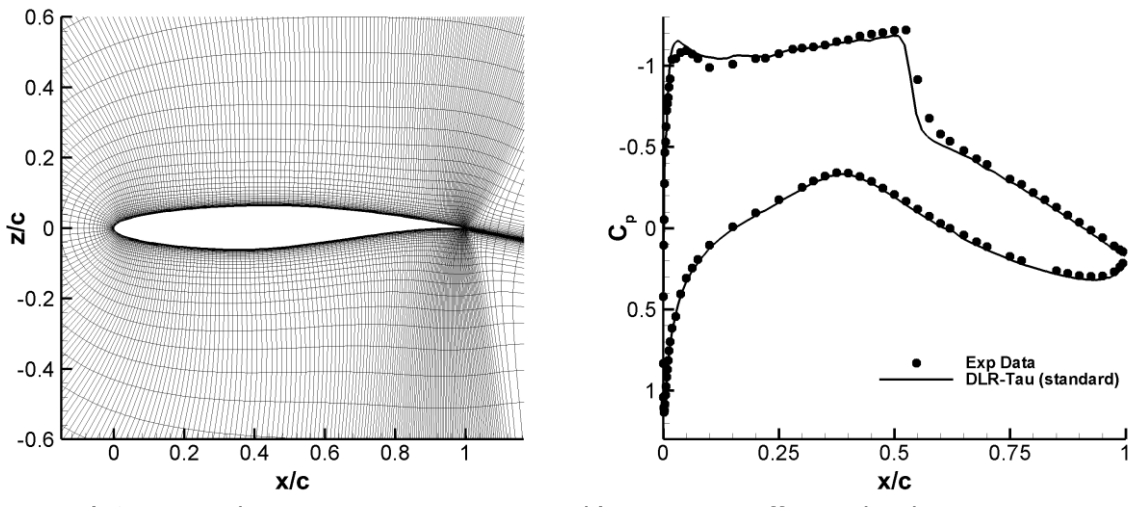


**Figure 1: Validation of RAE 2822 aerofoil; a) C-type structured grid; b) pressure coefficient distribution for Case 6.**

### 3.2 ONERA M6 Wing

The ONERA M6 wing is a swept wing with no twist, built with the symmetric ONERA D aerofoil. The computational grid is available from the validation web site of the NASA CFD code CFL3D [16]. The grid with  $288 \times 64 \times 48$  cells consists of one zone wrapped as a C-grid about the wing leading edge. Symmetry boundary condition was used on one side of the domain. The wing span features 256 cells in the chord-wise direction and 48 cells in the span-wise direction. The minimum wall distance of the first grid points off the wing surface is about  $2.5 \times 10^{-6}$  chords at the leading edge and about  $5 \times 10^{-6}$  chords at the trailing edge. The grid is non-dimensionalised by the span, and the mean aerodynamic chord is  $c = 0.54b$ .

Calculations were performed with the SA turbulence model. Experimental data are available for  $M = 0.84$  and Reynolds number, based on the mean aerodynamic chord,  $Re = 12.7 \cdot 10^6$  at a prescribed angle of attack  $\alpha = 3.06^\circ$  [17].

As for the aerofoil case, an explicit time stepping and the fourth order Runge-Kutta scheme were used. To accelerate the convergence to a steady state, a local time-stepping and implicit residual smoothing were used. The discretisation of the convective and diffusive fluxes of the RANS equations was based on the second order Roe's flux difference splitting scheme, and the first order accurate scheme was used for the SA fluxes. Venkatakrishnan's flux limiter was used. A no-slip boundary condition was set at the wing surface, and far-field boundary conditions were applied to the far-field boundaries. The CFL number was set to 1.2 and simulations were run for 20,000 iterations to compute the steady state solution. With this setup, the overall residuals of the NS and SA equations decreased by about five orders of magnitude, and all force and moment components converged within 15,000 iterations.

## 4 RESULTS

Uncertainty quantification and sensitivity analysis for the aerofoil test case are reported in Section 4.1. The Section continues with the calibration of the closure coefficients, discusses the implementation across different flow solvers, and investigates the influence of the spatial discretisation. Section 4.2 conveys that the optimal values of the closure coefficients improve slightly the solution for a complex flow around the wing test case.

### 4.1 RAE 2822 Aerofoil

#### Generation of the Response Surface Model

The computational framework described in Section 2 was used to generate a response surface model between the input parameters and the system outputs. The input parameters include nine uncertain closure coefficients of the SA turbulence model, which are described by the epistemic intervals in Table

1, and the angle of attack for matching the prescribed normal force coefficient. The system outputs that were monitored consist of three quantities: the lift and drag coefficients, and the sum of squared errors (*SSE*) between the pressure coefficient distribution from experimental data and that from numerical results. For uncertainty quantification and sensitivity analysis, and for the calibration of the closure coefficients, *SSE* is used as the output quantity of interest.

The generation of the response surface model followed the procedure:

1. the ADOE algorithm was initialised with 1,025 sample points selected by a two-level full factorial approach including the central point;
2. these results were then used to initialize the ADOE strategy and to compute sequentially an additional set of 1,500 CFD simulations. At the end of this step, the machine-learning framework identified automatically the best surrogate models to link the ten input variables to the system outputs based on a table containing 2,525 design points;
3. for each set of values of the closure coefficients included in this table, the surrogate models were interrogated to find the angle of attack that matched the target  $C_N = 0.743$ . By removing the dependence on the angle of attack, the 1,024 sample points of the full factorial plan were reduced to 512. Hence, this step reduced the size of the table to 2,013 sample points by adjusting the angle of attack to match the target  $C_N$ ;
4. finally, results at the previous step were validated by running a set of deterministic CFD simulations. Due to problems occurred on the local network connectivity, only 1,980 experiments out of 2,013 were successful and used to build the final surrogate models employed in the sensitivity analysis and calibration of the turbulence closure coefficients.

A total of 4,538 deterministic CFD simulations were run on the high-performance computing (HPC) facility of the University of Southampton (Iridis4) in just over 1,000 CPU hours. As an example, the Optimus simulation workflow is shown in Figure 2. This workflow integrates and automates the following main tasks that are performed during each iteration of the DOE / optimisation analyses:

1. map the value assigned to the turbulence coefficients within the input file required to run the CFD analysis;
2. submit the job with the instructions to launch the DLR-Tau flow solver to the resource manager of the HPC facility Iridis4, monitor its status and retrieve the output files upon job completion;
3. parse the output files to extract the values of the drag, lift, pitch moment, and pressure coefficients;
4. reorder the list of the calculated pressure coefficients to match those available from the experimental dataset;
5. calculate the mismatch between simulated and measured pressure coefficients in terms of the *SSE* metric.

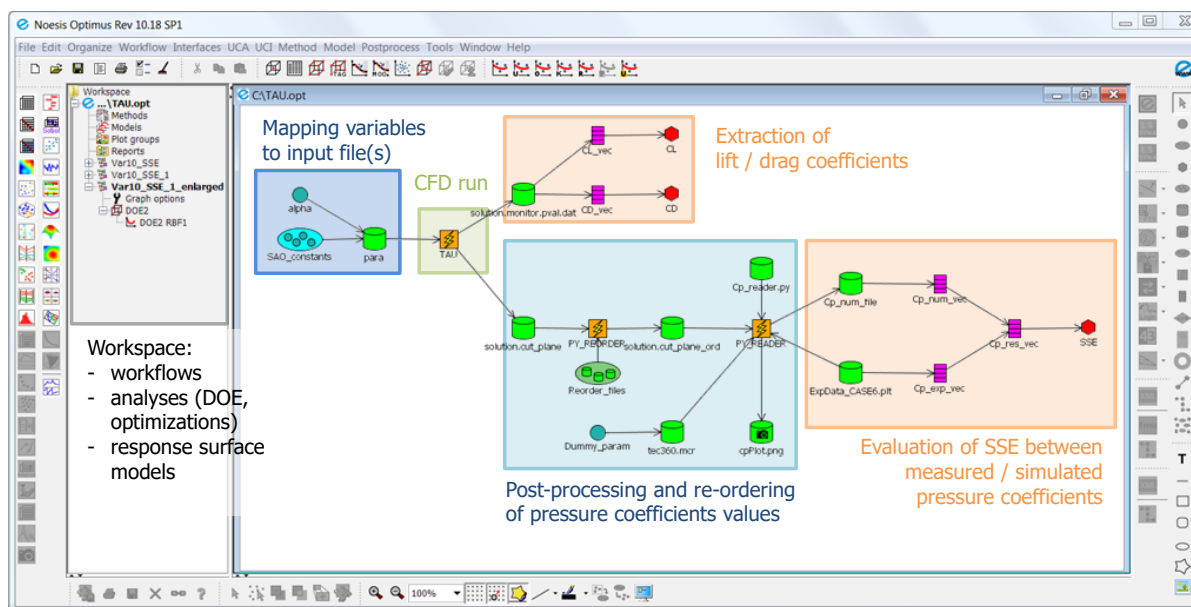


**Figure 2: Optimus workflow for the job submissions on the HPC facility and for running the ADOE and optimisation analyses.**



## Global Sensitivity Analysis

The global sensitivity analysis of the *SSE* between measured and simulated pressure coefficient on the uncertainty of the turbulence closure coefficients was analysed using the surrogate model generated with 1,980 sample points. The relative contribution of the input parameters to the total variability of *SSE* was quantified by relying on the variance-based Sobol indices [18]. Table 2 reports the values of the first order Sobol indices estimated via Monte Carlo integration performed with 10,000 random points evaluated on the surrogate model. In agreement with Ref. [4], the Von Karman constant,  $k$ , is the parameter that has the greatest impact on the variability of the system output. The mismatch between experimental data and numerical simulations is also influenced by the value of  $c_{v1}$  and, to a lesser extent, by  $c_{b1}$  and  $\sigma$ . The sensitivities with respect to the remaining five parameters ( $c_{w2}, c_{b2}, c_{t3}, c_{w3}, c_{t4}$ ) are virtually null. Being the value of the residual approximately equal to 0.01 (not reported in Table 2), no significant sensitivity can be attributed to the mutual interaction between the different input parameters. Results in Table 2 are not unexpected because the SA model consists of four nested versions, from the simplest which is applicable to free shear flows to the most complete, applicable to viscous flows past solid bodies and with laminar regions. The terms of each version are passive in all the lower versions of the model. The test case is for transonic wall-bounded flow, and only few terms of the SA model ( $k, c_{v1}, c_{b1}, \sigma$ ) are therefore active.

**Table 2: First order Sobol indices of the closure coefficients of the SA turbulence model with respect to SSE.**

Parameter	Sobol index
$k$	0.775
$c_{v1}$	0.111
$\sigma$	0.046
$c_{b1}$	0.046
$c_{w2}$	0.006
$c_{b2}$	0.004
$c_{t3}$	0.001
$c_{w3}$	0.001
$c_{t4}$	0.000

## Calibration of Turbulence Model Closure Coefficients

A two-steps approach was adopted to calibrate the closure coefficients of the SA turbulence model. The first step entails the identification of a global optimum by a differential evolution (DE) algorithm [19]. The DE is a genetic algorithm that is well-suited to find the global minimum of continuous functions, but at the cost of many expensive evaluation calls to reach convergence. To overcome this problem, the function evaluations were performed on the surrogate model, without the need to run the (expensive) CFD simulations. Because the DE algorithm is characterised by a non-deterministic behaviour, three separate runs initialised with different values of the random number generator seed were performed. This action was taken to mitigate the impact of the inherent randomness of the optimisation scheme on the obtained solution. Table 3 lists the optimum values of the turbulence model closure coefficients for the three optimisation runs. The five parameters with the lowest Sobol indices ( $c_{w2}$  through  $c_{t4}$ ) were kept at their nominal values. As expected, the optimum solutions found by the three test runs yield consistent results for the input parameters with the highest Sobol indices ( $k, c_{v1}, \sigma, c_{b1}$ ). These findings agree well with the set of optimised closure coefficients obtained through one of the deterministic CFD simulations executed during the DOE plan. Discrepancies on the remaining five parameters ( $c_{w2}$  through  $c_{t4}$ ) are non-influential, being their Sobol indices virtually null.

**Table 3: Optimal values of closure coefficients and corresponding SSE based on genetic algorithm evaluated on surrogate model and best experiment found during the DOE plan.**

Parameter	Optimisation run 1	Optimisation run 2	Optimisation run 3	Optimal DOE point
$k$	$3.600 \cdot 10^{-1}$	$3.600 \cdot 10^{-1}$	$3.600 \cdot 10^{-1}$	$3.610 \cdot 10^{-1}$
$c_{v1}$	$7.500 \cdot 10^0$	$7.500 \cdot 10^0$	$7.500 \cdot 10^0$	$7.431 \cdot 10^0$
$\sigma$	$9.970 \cdot 10^{-1}$	$1.003 \cdot 10^0$	$1.009 \cdot 10^0$	$1.163 \cdot 10^0$
$c_{b1}$	$1.400 \cdot 10^{-1}$	$1.400 \cdot 10^{-1}$	$1.400 \cdot 10^{-1}$	$1.380 \cdot 10^{-1}$
$c_{w2}$	$3.000 \cdot 10^{-1}$	$3.000 \cdot 10^{-1}$	$3.000 \cdot 10^{-1}$	$3.260 \cdot 10^{-1}$
$c_{b2}$	$6.220 \cdot 10^{-1}$	$6.220 \cdot 10^{-1}$	$6.220 \cdot 10^{-1}$	$6.260 \cdot 10^{-1}$
$c_{t3}$	$1.200 \cdot 10^0$	$1.200 \cdot 10^0$	$1.200 \cdot 10^0$	$1.963 \cdot 10^0$
$c_{w3}$	$2.000 \cdot 10^0$	$2.000 \cdot 10^0$	$2.000 \cdot 10^0$	$1.815 \cdot 10^0$
$c_{t4}$	$5.000 \cdot 10^{-1}$	$5.000 \cdot 10^{-1}$	$5.000 \cdot 10^{-1}$	$3.040 \cdot 10^{-1}$
SSE	$1.40 \cdot 10^{-1}$	$1.40 \cdot 10^{-1}$	$1.40 \cdot 10^{-1}$	$1.39 \cdot 10^{-1}$

The second step of the calibration procedure uses a gradient-based approach that launches additional deterministic CFD simulations. The non-linear programming quadratic line (NLPQL) optimisation scheme [20] was the method of choice. To mitigate the possibility of being entrapped in local minima, the algorithm is initialised from the optimal point found during the second global optimisation run and reported in Table 3. The optimal values of the closure coefficients are summarised in Table 4 after only one iteration that entailed 5 additional CFD simulations. It was found that the results of the gradient-based optimisation are virtually unchanged compared with the optimal values reported in Table 3. This reflects the good quality of the surrogate model generated by the machine-learning framework and provides also a validation of the overall optimisation approach, according to which: a) a large number of model evaluations performed on the surrogate model is firstly employed to find a global optimum; and b) a smaller number of CFD simulations is then used to refine the output of the calibration.

**Table 4: Optimal values of closure coefficients based on gradient-based algorithm evaluated on CFD simulations (SSE = 0.140).**

Parameter	Standard value	Calibrated value
$k$	$4.100 \cdot 10^{-1}$	$3.600 \cdot 10^{-1}$
$c_{v1}$	$7.100 \cdot 10^0$	$7.500 \cdot 10^0$
$\sigma$	$6.667 \cdot 10^{-1}$	$1.003 \cdot 10^0$
$c_{b1}$	$1.355 \cdot 10^{-1}$	$1.400 \cdot 10^{-1}$
$c_{w2}$	$3.000 \cdot 10^{-1}$	$3.000 \cdot 10^{-1}$
$c_{b2}$	$6.220 \cdot 10^{-1}$	$6.220 \cdot 10^{-1}$
$c_{t3}$	$1.200 \cdot 10^0$	$1.200 \cdot 10^0$
$c_{w3}$	$2.000 \cdot 10^0$	$2.000 \cdot 10^0$
$c_{t4}$	$5.000 \cdot 10^{-1}$	$5.000 \cdot 10^{-1}$

### Improved Prediction Accuracy

This section discusses two aspects related to the optimal values of the closure coefficients in Table 4. The first aspect is concerned with the improved prediction accuracy of the flow solution for Case 6. Figure 3a shows a comparison of the pressure coefficient obtained with the standard and calibrated SA models. Qualitatively, the solution with the optimal values of the closure coefficients improves the agreement with the experimental data near the leading edge and at the shock front. Quantitatively, the SSE is reduced from 0.206 for the standard SA model ( $\alpha = 2.51^\circ$ ) to 0.137 for the calibrated model ( $\alpha = 2.37^\circ$ ). The second aspect is about consistency and generality of the above conclusions across different flow solvers. For this purpose, two runs were performed with the SU2 flow solver [21] using the standard and calibrated SA models, on the same grid employed in DLR-Tau. Numerical settings were similar to those of DLR-Tau simulations. Figure 3b shows the pressure coefficient obtained with the standard and calibrated SA models in SU2. From the comparison, the improvement in prediction accuracy when using the calibrated model in SU2 is virtually identical to that observed in DLR-Tau. This confirms the above conclusions are consistent on different flow solvers, and so the advantages of using the calibrated turbulence model are solver-independent.

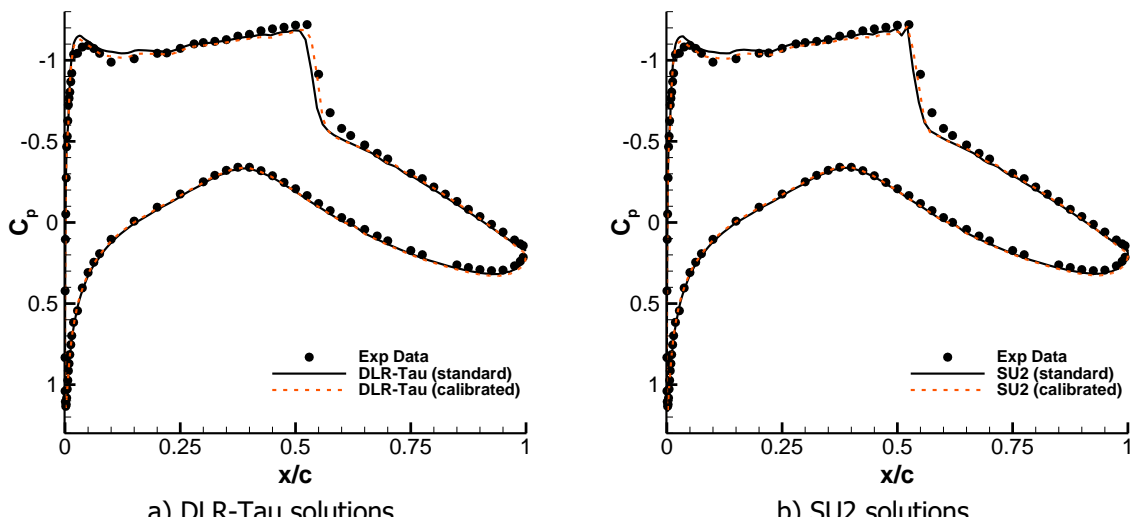


**Figure 3: Pressure coefficient with standard and calibrated SA turbulence model for Case 6 of RAE 2822 aerofoil, coarse grid.**

### Concluding Remarks

A finer grid was generated to investigate the influence of the spatial discretisation on the prediction capability for Case 6. The grid of Figure 4a, denoted hereafter the medium grid, consists of a single-block with  $865 \times 161$  points. The far-field boundary is placed at 50 chords from the aerofoil, and the distance of the first grid points off the aerofoil surface is about  $5 \times 10^{-6}$  chord.

As similarly observed for the pressure coefficient distribution on the coarse grid, the calibrated SA model achieves a better agreement with experimental data than the standard turbulence model. The comparison is reported in Figure 4b. A finer grid resolution improves significantly the pressure coefficient on the upper surface close to the leading edge and the shock position.

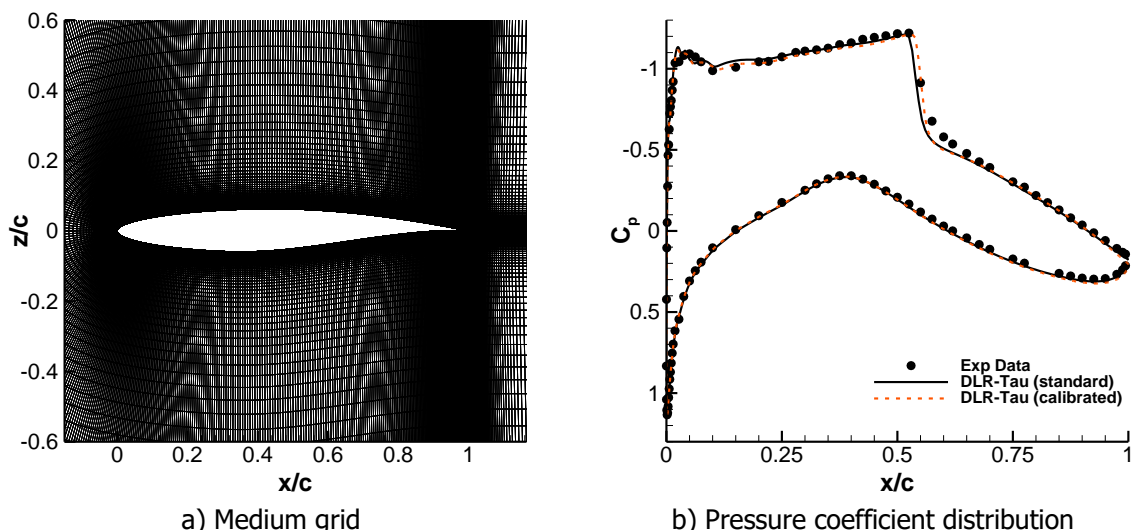


**Figure 4: Pressure coefficient with standard and calibrated SA turbulence model for Case 6 of RAE 2822 aerofoil, medium grid.**

A quantitative analysis of the influence of the spatial discretisation (coarse and medium grids) and of the turbulence model (standard and calibrated versions) on aerodynamic coefficients is summarised in Table 5. In all cases, the reported angle of attack is such that  $C_N = 0.743 \pm 0.0005$ . On the coarse grid, the solution of the calibrated SA model leads to good predictions of the drag and pitch moment coefficients. Taking as reference the experimental values, the percentage error in  $C_D$  is reduced from 18.1 to 7.9%, and the error in  $C_m$  from 4.2 to 1.1% when switching from the standard to the calibrated

turbulence model. Furthermore, results converge towards the experimental values as the grid is refined, for both versions of the turbulence model. On the medium grid, the solution of the calibrated SA model achieves an error of 2.3% in  $C_D$ , compared to 7.9% on the coarse grid. The pitch moment coefficient is unaffected by the spatial discretisation, with an error as small as 1.1%.

With the above paragraphs as background, one can identify different scenarios for the applicability of the current work. In a research scenario, the work can be used to determine the robustness of a turbulence model, and whether efforts should be addressed to improve the model in some way. In a design scenario, there is an interest to reduce the uncertainty arising from the turbulence modelling, or else to design a factor of safety around it. In a commercial scenario, the work could be used in a cost analysis, whereby uncertainty in drag coefficient will affect projected fuel costs.

**Table 5: Influence of spatial discretisation for standard and calibrated SA models on aerodynamic coefficients, Case 6.**

Exp Data	Coarse grid		Medium grid	
	Standard SA	Calibrated SA	Standard SA	Calibrated SA
$\alpha$ [°]	2.29	2.51	2.37	2.39
$C_D$ [counts]	127	150	137	142
$C_m$	-0.095	-0.091	-0.096	-0.092
				-0.096

## 4.2 ONERA M6 Wing

The pressure coefficients at six span-wise locations of the ONERA M6 wing are shown in Figure 5. The agreement with experimental data reveals the difficulty of a RANS solution to capture the double shock at 80% span-wise location and to predict the pressure coefficient in the cove region at 99% span-wise location. These deficiencies, commonly documented in the open literature, are attributed to physical modelling errors. The calibrated SA model has no effect in these two areas, suggesting that the deficiency is intrinsic to turbulence modelling and requires higher modelling fidelity in flow physics. By close inspection, the shock position and intensity of the calibrated SA model achieves a favourable agreement with experimental data, particularly, at locations 90 and 95% of the span. Although of limited extent, the solution of the calibrated SA model moves towards the reference data.

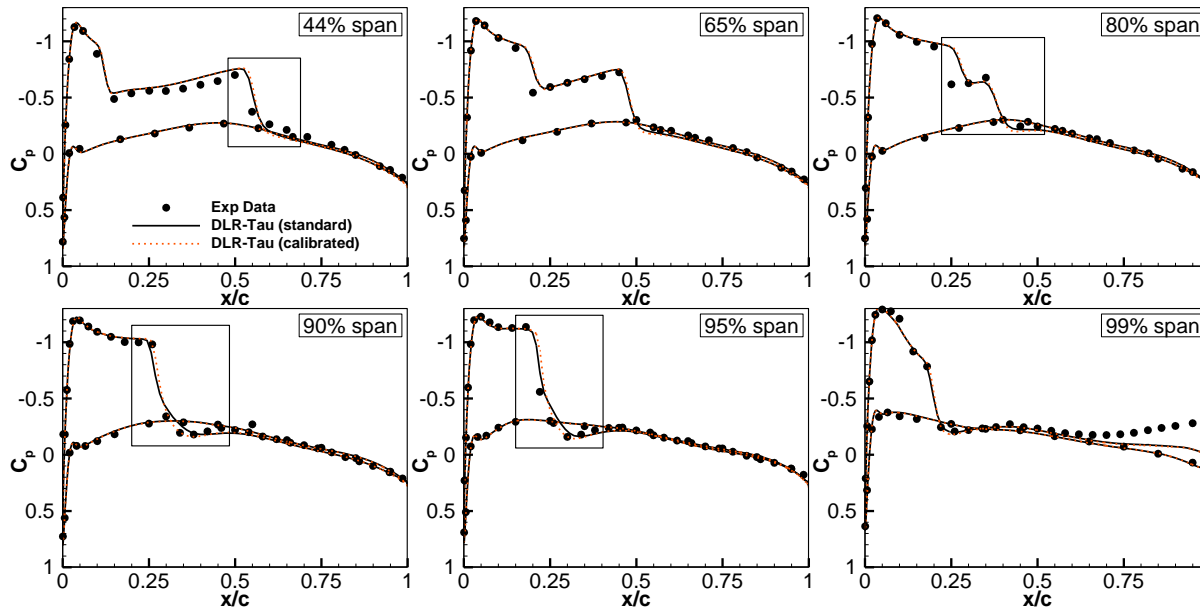


**Figure 5: Pressure coefficient with standard and calibrated SA turbulence model for ONERA M6 wing ( $M = 0.84$ ,  $Re = 12.7 \cdot 10^6$ ,  $\alpha = 3.06^\circ$ ).**

## 5 CONCLUSIONS

Uncertainty in the closure coefficients of a turbulence model is the dominant source of error in Reynolds-averaged Navier-Stokes simulations. This requires turbulence modelling uncertainty quantification and sensitivity analysis. The work detailed in this study addressed these aspects using state-of-the-art computational techniques, including a machine-learning software platform with an adaptive design of



experiments algorithm, a modern flow solver, and a high-performance computing facility. The original Spalart-Allmaras turbulence model was analysed. The key elements of this work are: a) uncertainty quantification and sensitivity analysis required only about 1,000 CPU hours to explore a ten-dimensional design space; b) only a selected number of closure coefficients have a large impact on the uncertainty of the output quantities of interest; this is not unexpected because the Spalart-Allmaras turbulence model has a nested structure, with the outer versions not altering the lower ones; c) the optimal values of the closure coefficients, which were implemented in a calibrated version of the Spalart-Allmaras model, were chosen to minimise the sum of square error of the pressure coefficient between experimental data and numerical results; d) the closure coefficients with the largest Sobol indices are determined accurately as they have the largest impact on the output quantities of interest. It was found that the calibrated Spalart-Allmaras turbulence model slightly outperforms the standard version for transonic, wall-bounded flows around the RAE 2822 aerofoil. The expected prediction accuracy holds for more complex transonic flows around the ONERA M6 wing, as well as across different flow solvers.

## ACKNOWLEDGMENTS

Da Ronch and Drofelnik gratefully acknowledge the financial support from the Engineering and Physical Sciences Research Council (grant number: EP/P006795/1).

Data supporting this study (grids, results, figures, etc.) are openly available from the University of Southampton repository at <https://doi.org/10.5258/SOTON/D0263>.

## REFERENCES

1. S. Hosder, R.W. Walters, M. Balch; 2010; "Point-Collocation Nonintrusive Polynomial Chaos Method for Stochastic Computational Fluid Dynamics"; *AIAA Journal*; **48**(12); doi: 10.2514/1.39389
2. J. Slotnick, A. Khodadoust, J. Alonso, D. Darmofal, W. Gropp, E. Lurie, D. Mavriplis; 2014; "CFD Vision 2030 Study: A Path to Revolutionary Computational Aerosciences"; *NASA/CR-20140218178*
3. S.C.C. Bailey, M. Vallikivi, M. Hultmark, A.J. Smits; 2014; "Estimating the Value of Von Karman's Constant in Turbulent Pipe Flow"; *Journal of Fluid Mechanics*, **749**; pp. 79-98
4. W.N. Edeling, P. Cinnella, R.P. Dwight; 2014; "Predictive RANS Simulations via Bayesian Model-Scenario Averaging"; *Journal of Computational Physics*, **275**; pp. 65-91.
5. P.R. Spalart, S.R. Allmaras; 1994; "A one-equation turbulence model for aerodynamic flows"; *La Recherche Aérospatiale*; **1**; pp. 5-21
6. D.I. Papadimitriou, C. Papadimitriou; 2015; "Bayesian Uncertainty Quantification of Turbulence Models Based on High-order Adjoint"; *Computers and Fluids*, **120**; pp. 82-97
7. J.A. Schaefer; 2015; "Uncertainty Quantification of Turbulence Model Closure Coefficients for Transonic Wall-bounded Flows"; *M.Sc. Thesis*; Missouri University of Science and Technology
8. P.H. Cook, M.A. McDonald, M.C.P. Firmin; 1979; "Aerofoil RAE 2822 – Pressure Distributions, Boundary Layer and Wake Measurements. Experimental Data Base for Computer Program Assessment"; *AGARD Report AR 138*
9. A. Da Ronch, M. Ghoreyshi, K.J. Badcock; 2011; "On the Generation of Flight Dynamics Aerodynamic Tables by Computational Fluid Dynamics"; *Progress in Aerospace Sciences*; **47**(8); pp. 597-620; doi: 10.1016/j.paerosci.2011.09.001
10. N.N. Sorensen; 2009; "CFD Modelling of Laminar-turbulent Transition for Airfoils and Rotors Using the  $\gamma - \widetilde{Re}_\theta$ "; *Wind Energy*, **12**; pp. 715-733; doi: 10.1002/we.325
11. A. Da Ronch, M. Panzeri, M.A. Abd Bari, R. d'Ippolito, M. Franciolini; 2017; "Adaptive Design of Experiments for Efficient and Accurate Estimation of Aerodynamic Loads"; *Aircraft Engineering and Aerospace Technology*, **89**(4); doi: 10.1108/AEAT-10-2016-0173
12. D. Schwamborn, T. Gerhold, R. Heinrich; 2006; "The DLR TAU-code: Recent Applications in Research and Industry"; *Proceedings of the European Conference on Computational Fluid Dynamics (ECCOMAS)*; September
13. A. Jameson, W. Schmidt, E. Turkel; 1981; "Numerical Solutions of the Euler Equations by Finite Volume Methods Using Runge-Kutta Time-stepping Schemes"; AIAA Paper 1981-1259; *14th Fluid and Plasma Dynamics Conference, Fluid Dynamics and Co-located Conferences*; Palo Alto, CA
14. Noesis Solutions; 2017; "Optimus Rev 10.19 - User's Manual"; *Technical Report*
15. NPARC Alliance Validation Archive:  
<https://www.grc.nasa.gov/WWW/wind/valid/raetaf/raetaf.html>



16. C.L. Rumsey; "Test/Validation Cases"; <http://cfl3d.larc.nasa.gov/>
17. V. Schmitt, F. Charpin; 1979; "Pressure Distributions on the ONERA-M6-Wing at Transonic Mach Numbers"; *Technical report*; Office National d'Etudes et Recherches Aerospatiales, 92320, Chatillon, France
18. I.M. Sobol; 2001; "Global Sensitivity Indices for Nonlinear Mathematical Models and Their Monte Carlo Estimates"; *Mathematics and Computers in Simulation*; **55**(1-3); doi: 10.1016/S0378-4754(00)00270-6
19. R. Storn, K. Price; 1997; "Differential Evolution – A Simple and Efficient Heuristic for Global Optimization Over Continuous Spaces"; *Journal of Global Optimization*; **11**(4); pp. 341-359; doi: 10.1023/a:1008202821328
20. K. Schittkowski; 1986; "NLPQL: A Fortran Subroutine for Solving Constrained Nonlinear Programming Problems"; *Annals of Operations Research*; **5**(2); pp. 485-500; doi: 10.1007/BF02022087
21. T.D. Economon, F. Palacios, S.R. Copeland, T.W. Lukaczyk, J.J. Alonso; 2015; "SU2: An Open-Source Suite for Multiphysics Simulation and Design"; *AIAA Journal*; **54**(3); pp. 828-846